University of Baghdad
College of Engineering
JOURNAL OF ENGINEERING

Journal of Engineering

journal homepage: www.joe.uobaghdad.edu.iq

Volume 29 Number 12 December 2023

Simulation and Experimental Investigation of Performance and Flow Behavior for Steam Ejector Refrigeration System

Shakir J. Jasim[1,*], Akram W. Ezzat[2], Eric Hu[3]

[1,2] Department of Mechanical Engineering, College of Engineering, University of Baghdad, Baghdad, Iraq
[3]Mechanical Engineering School, University of Adelaide SA 5005, Australia
Shakir.alsaeedi@gmail.com[1], akram.w@coeng.uobaghdad.edu.iq[2], Eric.hu@adelaide.edu.au[3]

ABSTRACT

The ejector refrigeration system is a desirable choice to reduce energy consumption. A Computational Fluid Dynamics CFD simulation using the ANSYS package was performed to investigate the flow inside the ejector and determine the performance of a small-scale steam ejector. The experimental results showed that at the nozzle throat diameter of 2.6 mm and the evaporator temperature of 10°C, increasing boiler temperature from 110°C to 140°C decreases the entrainment ratio by 66.25%. At the boiler temperature of 120°C, increasing the evaporator temperature from 7.5 to 15 °C increases the entrainment ratio by 65.57%. While at the boiler temperature of 120°C and the evaporator temperature of 10°C, increasing the nozzle throat diameter from 2.4 to 2.8 mm decreases the entrainment ratio by 40%. The numerical results showed that reducing the condenser back pressure or increasing the primary fluid temperature, secondary fluid temperature, and nozzle throat diameter moves the second shock waves in the downstream direction. It could be concluded that the second shock series position detects the ejector operation mode. The ejector runs in critical mode if the second shock series position is close to the diffuser. In contrast, if the second shock series position moves toward the upstream, the ejector runs in subcritical mode.

Keywords: Experimental test, Numerical simulation, Steam ejector, Shock waves, System performance.

*Corresponding author
Peer review under the responsibility of University of Baghdad.
https://doi.org/10.31026/j.eng.2023.12.02

Article received: 02/04/2023
Article accepted: 22/10/2023
Article published: 01/12/2023

المحاكاة والتحقيق التجريبي للأداء وسلوك الجريان لنظام التبريد بقاذف البخار

شاكر جواد جاسم[1]* ، اكرم عزت وهبي[2]، أريك هو[3]

[1،2] قسم الهندسة الميكانيكية، كلية الهندسة، جامعة بغداد، بغداد، العراق

[3]الهندسة الميكانيكية، جامعة اديلايد، استراليا

الخلاصة

يعد نظام التبريد بالقاذف خيارًا مرغوبًا لتقليل استهلاك الطاقة. تم إجراء محاكاة باستخدام حزم (CFD ANSYS) للتحقق من التدفق داخل القاذف وتحديد أداء قاذف البخار صغير الحجم. اظهرت النتائج التجريبية أنه عند قطر عنق المنفث 2.6 مم ودرجة حرارة المبخر 10 درجة مئوية، تؤدي زيادة درجة حرارة المرجل من 110 درجة مئوية إلى 140 درجة مئوية إلى تقليل نسبة االسحب بنسبة 66.25٪. عند درجة حرارة المرجل 120 درجة مئوية، تؤدي زيادة درجة حرارة المبخر من 7.5 درجة مئوية إلى 15 درجة مئوية إلى زيادة نسبة السحب بنسبة 65.57٪. بينما عند درجة حرارة المرجل البالغة 120 درجة مئوية ودرجة حرارة المبخر 10 درجة مئوية، فإن زيادة قطر عنق المنفث من 2.4 مم إلى 2.8 مم تقلل نسبة السحب بنسبة 40٪.أظهرت نتائج المحاكات أن خفض الضغط الخلفي للمكثف أو زيادة درجة حرارة المائع الأولي ودرجة حرارة السائل الثانوي وقطر فوهة المنفث أدى إلى تحريك موجات الصدمة الثانية إلى اتجاه مخرج الناشر. يمكن الاستنتاج أن موضع سلسلة الصدمات الثانية يكشف وضع تشغيل القاذف. يعمل القاذف في الوضع الحرج إذا كان موضع سلسلة الصدمات الثانية قريبًا من الناشر. في المقابل إذا تحرك موضع سلسلة الصدمات الثانية باتجاه المنفث فان القاذف يعمل في الوضع دون الحرج.

الكلمات المفتاحية: الاختبار التجريبي، المحاكاة العددية ، قاذف البخار، موجات الصدمة, أداء المنظومة.

1. INTRODUCTION

The use of cooling systems to promote human comfort has increased energy consumption during the previous several decades. Air conditioning systems use the most significant proportion of overall energy. Ejector refrigeration supplied by solar thermal energy is the best choice for vapor compression refrigeration (**Luis and Christine, 2008; Kim and Infante, 2008)**. The primary drawbacks of ejector refrigeration systems are their low coefficient of performance (COP) and the challenges in ejector design, which severely limit the system's broad applicability **(Chunnanond and Aphornratana, 2004; Chen, 2014)**. Several research projects on the ejector refrigeration system have been developed to understand its properties better and promote its uses **(Rashid et al., 2022).** Ejector prototype testing is widely acknowledged as the most definitive method for determining performance. The significant expense of such an attempt, however, demands the development of other methods for assessing the performance of ejectors. Numerical modeling has become a feasible method for improving the performance of ejectors with the high growth of Computational Fluid Dynamics (CFD) capabilities. It is a good tool for analyzing the effects of shape and operation conditions **(Galindo et al., 2020).**

(David et al., 2008; Yu et al., 2019b) developed a supersonic ejector model using commercial CFD. The model used R141b and R245fa as refrigerants. Utilizing the refrigerant's real-gas properties was a significant aspect of the model. The developed CFD model produced a maximum discrepancy of 10.8% between the proposed model and the

actual data across all situations investigated. The findings demonstrated that the nozzle output location, evaporator inlet diameter, and mixing length seemed to have little effect on ejector performance. **(Natthawut et al., 2013)** investigated the impact of the primary nozzle geometries on the ejector performance of a steam refrigeration cycle using CFD software. The operation conditions used in the study were the evaporator temperature of 7.5°C and boiler temperatures of (110–150°C). The main nozzle throat diameters (1.4-2.6 mm) with an exit Mach number of 4 were set. Three nozzles were used, each with a different exit Mach number of 3.0, 4.0, and 5.5; the throat diameter of each nozzle was 1.4 mm. The finding showed that the optimum condition was the primary nozzle with a throat diameter of 2.3 mm and exit Mach number of 4 with the boiler temperature of 120 °C at the evaporator temperature of 7.5 °C. This study concluded that the CFD technique could be used as an efficient tool to predict the performance of a steam ejector. The outcomes also showed that the main nozzle configuration and the operation conditions significantly affected the performance of the ejector and, therefore, the COP of the system. **(Federico et al., 2016)** investigated the consequences of non-equilibrium condensation in a supersonic stream of pure steam using a commercial CFD package (ANSYS) simulation. The boiler temperature was 80°C, the superheating temperature was (60–10)°C, the evaporator temperature was 10°C, and the condenser temperature was 39°C. The results showed that overlooking the condensation phenomenon can lead to inaccurate results, perhaps resulting in incorrect ejector geometry sizing. This condensation may result in inaccurate predictions of the entrainment ratio of the ejector, pressure losses, and maximum sustainable condenser pressure. Condensation, in particular, reduces the Mach number along the main nozzle, affecting the main flow's expansion level. This condensation may result in inaccurate predictions of the entrainment ratio of the ejector, pressure losses, and maximum sustainable condenser pressure.

(Masoud et al., 2018) conducted a numerical CFD (fluent) package simulation to explore the influence of each geometrical parameter (nozzle exit position (NXP), the main nozzle divergent angle, and secondary throat length) on ejector performance. The pressure-based solver and RNG K-Ɛ turbulence model were employed in the simulation. A real gas model was utilized as the equation of state to account for the probability of water phase changes while flowing through the ejector. The results demonstrated that the entrainment ratio might be achieved largely within the analyzed intervals of the selected geometrical parameters, such as the primary nozzle divergence angle and the NXP. Other factors, such as the exit diffuser's divergence angle, influence the ejector's entrainment ratio less. **(Yu et al., 2019a)** investigated the interior shock wave configuration of the ejector using CFD simulation. The simulation was carried out using density-based and realizable K-Ɛ turbulence models. The primary fluid pressure was 360,000 Pa; the secondary fluid pressure was 2330 Pa, back pressure was 3500 Pa. According to numerical predictions, the entrainment ratio increases under two conditions: (1) when a normal shock wave reaches the exit and (2) a larger pseudo-shock zone. **(Suvarnakuta et al., 2020)** investigated the two-stage steam ejector performance using CFD. The two-stage ejector was simulated using boiler temperature in the range of (100–130°C) and evaporator temperature in the range of (0–15°C). According to the modeling results, the two-stage ejector offered a high entrainment ratio of about 77.2% while exhibiting a marginal drop in critical back pressure of approximately 21.9%. As a result, the two-stage ejector may considerably benefit refrigeration systems that need a high cooling load while maintaining a low pressure on the condenser. **(Wenxu et al., 2021)** utilized a CFD simulation to streamline the primary nozzle

structure of the ejector structure. Two distinct streamline forms of the nozzle convergent and divergent sections were studied, and 16 possible nozzle profiles with all diameters and lengths were constructed. The results demonstrated that the suggested streamline nozzle works better when the primary pressure is inadequate. At the main flow pressures of 4.5 and 5.5 bar, the entrainment ratios of an ejector with a streamlined nozzle of convex-straight line shape (profile B2T) were approximately 19.79% and 8.04%, respectively, more significant than the ejector with a baselined nozzle of the straight-straight line shape.
In the present work, a two-dimensional numerical simulation (ANSYS Fluent 19.2) was used to investigate the flow behavior and mixing activities in parts of the ejector that cannot be reached by experiment or analytical 1-dimensional studies and get an acceptable ejector performance. A small-scale ejector using water as a working fluid was used at different operating conditions and nozzle throat diameters.

2. EJECTOR THEORY

An ejector is a flow device that has no moving components. Instead, the ejector uses the momentum of a fast primary fluid to entrain and pump a slow secondary fluid **(Ezzat and Addaiy, 2010**). The ejector, boiler, and pump are used instead of a compressor in a vapor-compression system to provide cooling power in an ejector refrigeration system.
The performance of the ejector is often evaluated based on a mass flow ratio that compares the streams coming from the generator and the evaporator **(Sun, 1999; Yapıcıa et al., 2008)**. This ratio, known as the entrainment ratio (ω), is limited by the condenser back pressure (P_c) at a certain secondary pressure (P_s) and primary pressure (P_p). According to the back pressure, there are three operation modes. The critical mode performs best when the back pressure is less than the critical pressure. In this situation, the entrainment ratio is constant, and choking occurs in the main and entrained flows. When the back pressure exceeds the critical pressure, the entrainment decreases; choking occurs only in the main flow but not the secondary one. If the back pressure exceeds P_{co}, as shown in **Fig. 1,** there will be no choking in either flow. P_{co} is regarded as the limiting pressure of the ejector's operational mode. The operation would then fail. The following study begins with the expansion of the main flow through the nozzle, then the evaluation of secondary and mixed flow at various cross sections, and finally, the flow through the diffuser **(Hart, 2002; Jamal and Ezzat, 2021)**.
The coefficient of performance (COP), which is the ratio of the valuable cooling or refrigeration effect at the evaporator to the gross energy input into the cycle necessary to create the cooling effect **(Jassim and Abid 2016; Sokolov and Hershgal, 1990**), is used to evaluate the thermodynamic performance of the ejector compression cycle. Therefore, COP is given by:

$$COP = Q_e/(Q_b + W_p,) \quad (1)$$

Q_e represents the cooling load in the evaporator, Q_b represents energy added to the boiler, and W_p represents the electrical consumption in the pump.
The ejector performance is characterized by the entrainment ratio (ω), representing the mass flow rate ratio between the evaporator and boiler streams, such that :

$$\omega = \frac{\dot{m}s}{\dot{m}p} \quad (2)$$

where $\dot{m}_s$ is the secondary mass and $\dot{m}_p$ is the primary flow.

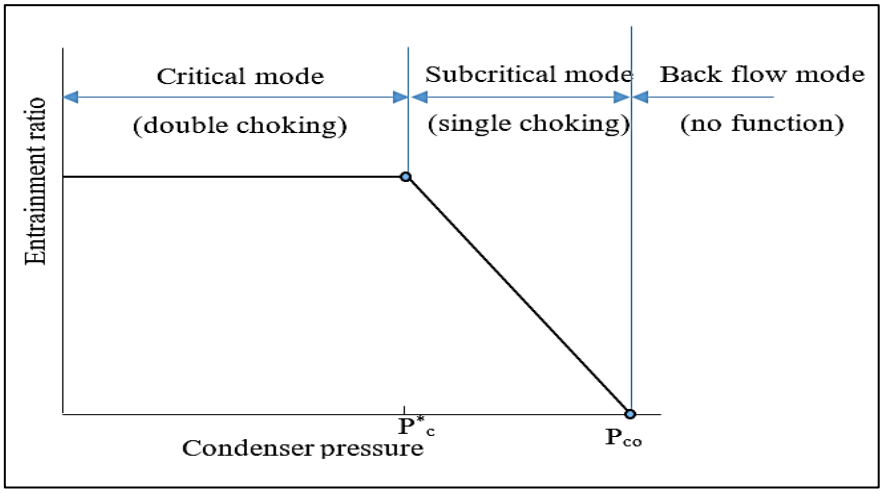

Figure 1. Ejector operation modes **(Hart, 2002)**

3. EXPERIMENTAL WORK

3.1 Test Rig Description

A proper experimental test rig is designed, fabricated, and integrated to understand better the contribution of design and operational parameters that affect the coefficient of performance related to steam ejector cooling systems. This rig (shown in **Fig. 2**) is intended to be reasonably compact, with a cooling capability of around 1 kW.

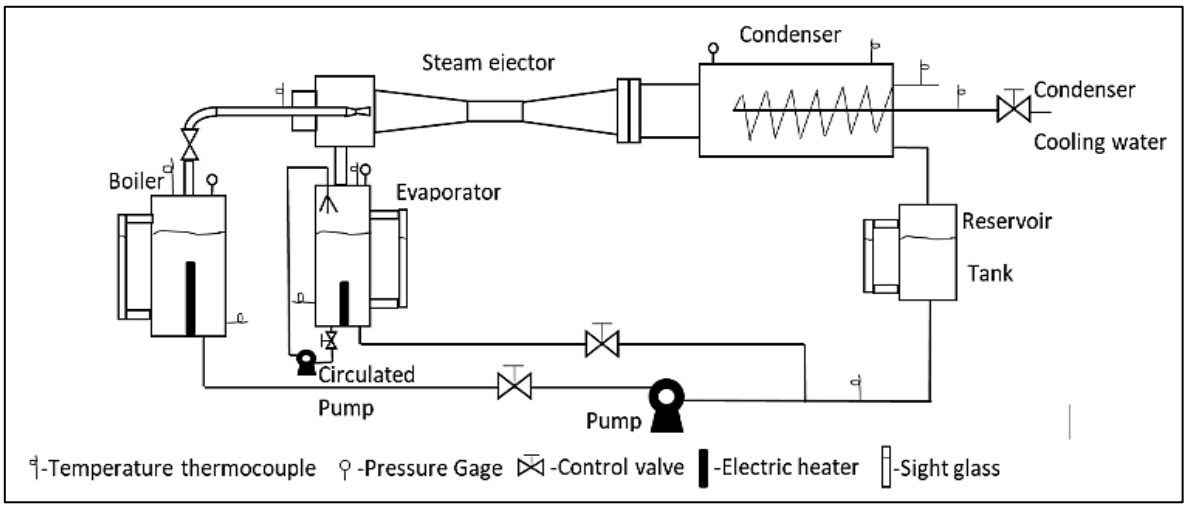

Figure 2. Schematic diagram of experimental steam ejector system.

The device comprises a supersonic ejector, a steam generator, an evaporator, a condenser, pumps, valves, and measuring tools like thermocouples, pressure gauges, and sight glasses to assess system performance.

Experimental work based on the primary steam saturation temperatures of (110-140^{o}C) is generated by a 7.5 kW electric heater controlled by a voltage regulator. The secondary steam temperatures used in the test were about (7.5- 15^{o}C), depending on the cooling load. The

cooling load is represented by a 2 kW electric heater controlled by a voltage regulator to adjust the specified secondary steam temperature. The temperature of the condenser was in the range of (25-45^{o}C), which is governed by the mass flow rate of the condenser cooling water. Aluminum was used to manufacture the ejector and the nozzle, while carbon steel was used to manufacture the other parts of the rig test.

Figure 3. A photograph of the Rig test

3.2 Error Analysis

Errors and uncertainties are inherent in any measurement and in the instrument with which measurements are made. Error analysis is essential to investigate their effects on measurement outputs and the required solutions for reducing them. The experimental results' accuracy is determined by measurement accuracy and the capability and manufacturing of the test rig to match the experimental conditions and input data.
Undoubtedly, the maximum portion of calculation errors referred essentially to the errors in the measured quantities. Hence, to calculate the error in the obtained results, the Kline and McClintock (**Holman 2020**) method is used in this field. Let R be a function of n independent variables (v_1, v_2....,v_n).

$$R=R(v_1,v_2 \ldots\ldots v_n) \quad (3)$$

For minor variations in the variables, this relation can be expressed in linear form as:

$$\delta R = \frac{\partial R}{\partial v_1}\delta V_1 + \frac{\partial R}{\partial v_2}\delta V_2 + \cdots + \frac{\partial R}{\partial v_n}\delta V_n \quad (4)$$

Hence, the uncertainty interval (w) in the result can be given as follows:

$$w_R = \left[\left(\frac{\partial R}{\partial v_1} w_1\right)^2 + \left(\frac{\partial R}{\partial v_2} w_2\right)^2 + \cdots + \left(\frac{\partial R}{\partial v_n} w_n\right)^2\right]^{0.5} \quad (5)$$

Eq. 5 is greatly simplified upon dividing by Eq. 4 to non-dimensional:

$$\frac{w_R}{R} = \left[\left(\frac{w_1}{R}\right)^2 + \left(\frac{\partial R}{\partial v_2}.\frac{w_2}{R}\right)^2 + \cdots + \left(\frac{\partial R}{\partial v_n}\frac{w_n}{R}\right)^2\right]^{0.5} \quad (6)$$

Hence, the experimental errors that may exist in the independent parameters are given in **Table 1**. These uncertainties are taken from measuring devices as follows:

Table 1 Uncertainties of Measuring Tools

Independent parameter	Uncertainty value
Density(p)	+0.02 kg/m^3
Time(t)	+0.01 sec
Height(h)	+0.0001m
Diameter(d)	+0.0001m

The mass flow rate equation could be written as follows:

$$\dot{m} = \rho * Q = \rho * \frac{A*h}{t} \quad (7)$$

The experimental error in the mass flow rate can be expressed in the following manner:

$$\frac{\partial \dot{m}}{\partial \rho} = \frac{Ah}{t} \quad (8)$$

$$\frac{\partial \dot{m}}{\partial A} = \frac{\rho h}{t} \quad (9)$$

$$\frac{\partial \dot{m}}{\partial h} = \frac{\rho A}{t} \quad (10)$$

$$\frac{\partial \dot{m}}{\partial t} = -\frac{\rho h A}{t^2} \quad (11)$$

Therefore, the uncertainty intervals (w) in the result can be given as follows:

$$w_{\dot{m}} = \left[\left(\frac{\partial \dot{m}}{\partial \rho} w_\rho\right)^2 + \left(\frac{\partial \dot{m}}{\partial A} w_A\right)^2 + \left(\frac{\partial \dot{m}}{\partial h} w_h\right)^2 + \left(\frac{\partial \dot{m}}{\partial t} w_t\right)^2\right]^{0.5} \quad (12)$$

To calculate the error in the primary mass flow rate as a sample of calculation for the given below information, the flowing procedure can be followed;

$\dot{m}_p$=0.00166kg/sec ρ=943 kg/m^3 A=32.41*10^{-3} m^2 h=0.025 m t=460 sec

$\frac{\partial \dot{m}p}{\partial \rho}$=1.76*10^{-6},

$\frac{\partial \dot{m}}{\partial A}$=5.12*10^{-2},

$\frac{\partial \dot{m}}{\partial h}$=6.64*10^{-2},

$\frac{\partial \dot{m}}{\partial t}$=-3.6*$10^{-6}$

$w_{\dot{m}p} = [(1.76 * 10^{-6} * 0.02)^2 + (5.12 * 10^{-2} * 10^{-4})^2 + (6.64 * 10^{-2} * 10^{-4})^2 + (-3.6 * 10^{-6} * 10^{-2})^2]^{0.5}$ =8.38*10^{-6}

3.3 Experimental Procedure

The test rig is evacuated using a vacuum compressor until the test rig pressure reaches saturated vapor pressure related to water temperatures inside the boiler, condenser, and evaporator. The primary flow stream, which has high pressure, enters the ejector's main nozzle and induces the evaporator's low-pressure vapor (secondary flow). The condenser coil is supplied with cooling water. The mixed vapor is cooled by cooling water in the condenser, and then the condensed water flows by the effect of gravity. When the temperature of the evaporator drops, the recirculation pump of the evaporator is turned on to shorten the elapsed time required to reach a steady state .The evaporator heater, which represents the cooling load, is turned on and regulated by a voltage regulator to maintain the required evaporator temperature. After establishing the steady-state condition, which takes about 30 minutes, all the conducted measurements are realized. The water collected from the condenser is then fed back to the boiler and the evaporator.

4. NUMERICAL SIMULATION

The advancement of computational power led to the development of ejector design codes capable of solving differential equations. Constant pressure and constant area models are one-dimensional approaches to ejector design. Many assumptions were made in these approaches, causing the method to be inaccurate **(Varga et al., 2012; Fletcher, 2013).** The two-dimensional method is more accurate than the one-dimensional method, but the complicated equations make it challenging to implement in design optimization. The technique was ruled out as an effective method because of the many empirical coefficients required. Although more complex, costly, and time-consuming than mathematical models, numerical models can accurately estimate flow phenomena, such as shock waves, mixing, and complex flows. The selection of the physical model, particularly the turbulence model, and the mesh quality are the two most important factors affecting the problem's definition **(Diogo, 2019)**. When properly implemented, CFD is a low-cost and rapid testing method. As a design tool, it facilitates the optimization of a process with high reliability and at a fraction of the cost and time required by conventional design methods, which require the fabrication of multiple prototypes (**Megdouli et al., 2015)**.

5. SUPERSONIC FLOW PHENOMENA

A significant amount of complexity is added to the situation due to the interaction between subsonic and supersonic mixing, the impact of expansion fans, and shockwaves embedded inside the supersonic motive jet. The influence of the process imposed upon it by the closeness of the shroud wall adds a layer of complexity to it. The main fluid stream is accelerated to supersonic speed in the nozzle diverging section when it passes through the main nozzle. The main fluid exits the main nozzle at a supersonic speed for Mach number Ma

of 4, and the flow at free boundary pressure. Consequently, an extended wave with some expansion angle is created **(Hart, 2002)**. The expanded wave may be divided into two types: over-expanded waves and under-expanded waves **(Sriveerakul et al., 2007)**.

The main flow departs the nozzle with a divergence of an expansion angle in the case of an under-expanded wave, as illustrated in **Fig. 4**. This happens when the pressure at the nozzle outlet exceeds the pressure in the mixing chamber **(Matsuo et al., 2013)**. The jet stream expands more after reaching the nozzle's exit plane due to the impact of an under-expanded wave, resulting in a greater supersonic level. This results in the appearance of a diamond wave. The differential pressure between the mixing chamber and the nozzle output influences the expansion angle and supersonic level.

If the wave is over-expanded, the main fluid will exit the primary nozzle with a convergent expansion angle, as seen in **Fig. 5**. When the static pressure at the main nozzle exit is lower than the static pressure in the mixing chamber, this occurs. A diamond wave and a series of oblique shock waves are formed, like in the under-expanded wave case. On the other hand, the oblique shock is not nearly as strong as an under-expanded wave. Consequently, the jet stream's flow is more stable, and the main fluid's supersonic speed after exiting the nozzle remains almost constant. As a result, the overall loss of jet stream momentum is smaller than that of an under-expanded wave **(Natthawut et al., 2013)**.

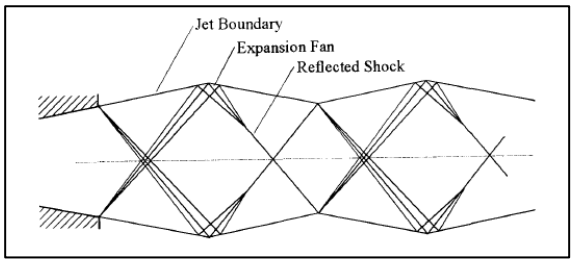

Figure 4. Under-Expanded jet wave **(Hart, 2002)**

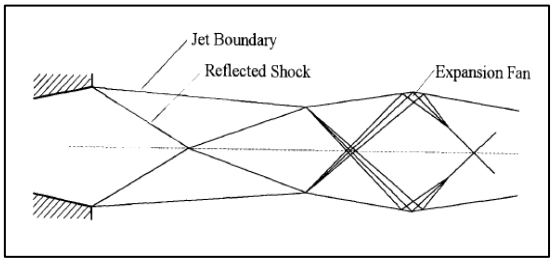

Figure 5. Over-Expanded jet wave **(Hart, 2002)**

6. CFD MODELING

The CFD tool computes the mathematical model of the physical problem using physical principles such as governing equations and other assumptions. Most CFD models solve the compressible Navier-Stokes equations **(Robert, 2010)**. The assumptions were: the flow is two-dimensional, steady state, Compressible turbulent flow, and the flow assumed to be single phase, a real gas. The following equations were used to find values for the three crucial unknown variables.

$$\text{Continuity: } \frac{D\rho}{Dt}\rho - \text{div}\,\nu = 0 \tag{13}$$

$$\text{Momentum: } \rho\frac{\partial}{\partial t}(\rho\,\nu_i) + \rho\frac{\partial}{\partial x_j}(\rho\,\nu_i\nu_j) = -\frac{\partial p_i}{\partial x_i} + \frac{\tau_{ij}}{\partial x_j} + \frac{\partial}{\partial x_j}(-\rho\,\overline{\acute{\nu}_i\acute{\nu}_j}) \tag{14}$$

$$\text{Energy: } \rho\frac{Dh}{Dt} = \frac{DP}{Dt} + \text{div}(k\nabla T) + \tau_{ij}\frac{\partial \nu_i}{\partial x_i} \tag{15}$$

The term τ_{ij} in equations 14 and 15 represents the viscous flow tension in ij, general space coordinates (2-D), and it can be written as

$$\tau_{ij} = 2\mu S_{ij} \quad (16)$$

where μ is the fluid's dynamic viscosity, and S_{ij} is the strain rate tensor.
The strain rate tensor is defined as follows:

$$S_{ij} = \frac{1}{2}\left(\frac{\partial v_i}{\partial x_j} + \frac{\partial v_j}{\partial x_i} - \frac{2}{3}\frac{\partial v_k}{\partial x_k}\delta_{ij}\right) \quad (17)$$

7. CFD METHODOLOGY

In this research, the ejector was split into 14 blocks to produce the shape of the steam ejector, as shown in **Fig. 6**.

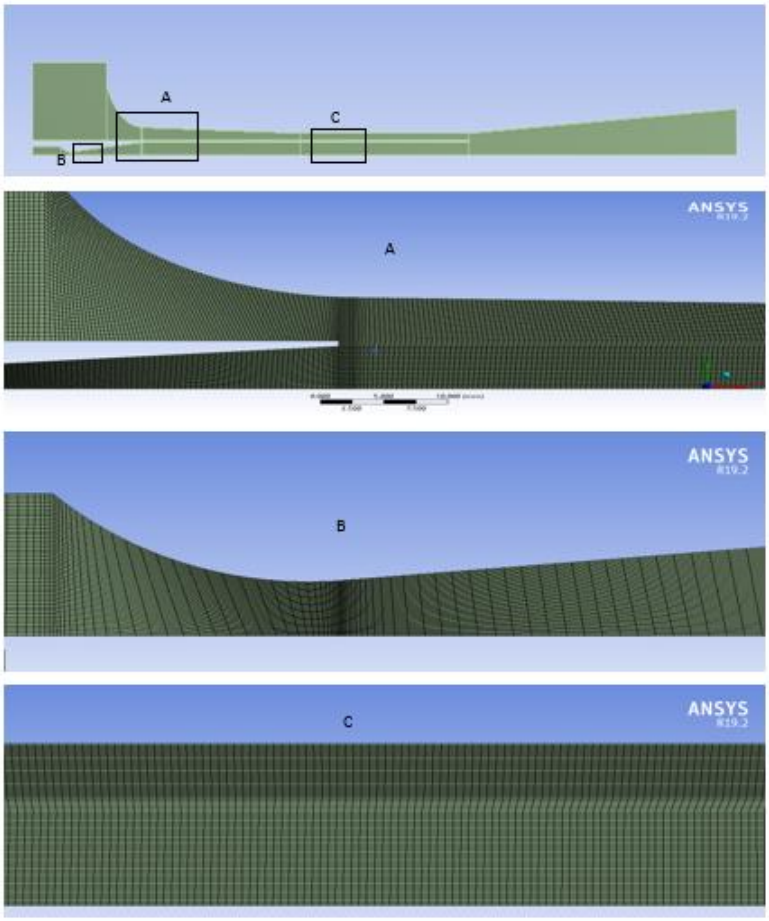

Figure 6. Grids used through ejector at different sections

The ejector's two inlets and one exit were subjected to boundary conditions. 'Subsonic inlet' boundary conditions were specified at sites where the high pressure and temperature of the main stream enter the ejector by a converging-diverging nozzle, and the low temperature and pressure of the secondary stream enters the ejector through a plenum chamber. The grid elements through the ejector were increased to about 110,000 elements to ensure the results (secondary and primary mass flow rate) are independent of the number of grid elements. The ejector geometry shown in **Fig. 7**, applied in this study with three different

supersonic nozzle throat diameters size (2.4, 2.6, and 2.8 mm), and different motive-stream operating conditions were simulated as summarized in **Table 2**.

Table 2. Operation conditions specified in the ejector simulation

Position	Pressure (kPa absolute)	Temperature (°C)
Primary stream	143.2, 198, 270, 360	110, 120, 130, 140
Secondary stream	1.03, 1.228, 1.7	7.5, 10, 15
Condenser condition	3.169-9.59	25-45

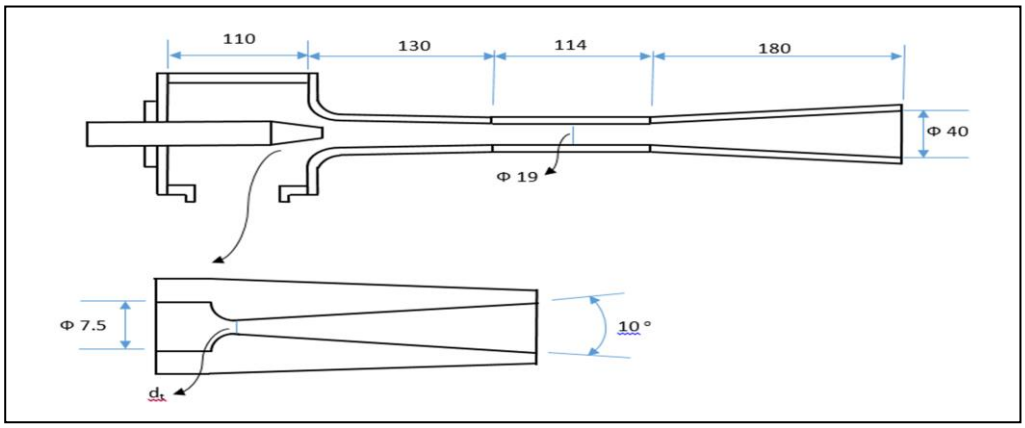

Figure 7. Sketch and dimensions of the ejector and the supersonic nozzle

The only reasonable simplifying assumption made is that the model is axisymmetric. In a 2-D axisymmetric, the circumferential derivatives of flow variables (pressure and velocity) are zero. As the ejector's geometry is symmetric, a 2-D axis-symmetric model was used. A steady-state fluid flow was established, and the pressure-based solver was chosen to provide results equivalent to those of the density-based solver while being significantly more stable and having a quicker convergence rate **(Nguyen and Vuaand, 2018**).

The flow within the ejector is often considered to correspond to turbulent compressible flow since it was previously thought to be in a supersonic flow field. The realizable k-Ɛ model has been extensively validated for many flows, including jets and mixing layers **(Huang et al., 1999**). In these cases, the model's performance was significantly better than the standard model's. The k-ω Turbulence Models require a high mesh resolution near the wall and have difficulty convergent depending on the initial conditions **(Riffat and Everitt, 1999)**. Thus, the standard wall function was applied for the wall, and the Realizable K-Ɛ Model was selected for the turbulence model. Proper boundary conditions must be set to solve the governing equations. The primary and secondary inlet pressure and temperature and the outlet pressure and temperature are provided and directly applied as BCs. This providing was a reasonable option when the transport losses between the ejector outlet and the condenser were assumed to be negligible. The simulations were carried out using water vapor as the fluid, and a real gas compressible steady-state form of the conservation equation governs the flow **(Ezzat, 1980)**. The second-order method was used for reasonable accuracy for pressure, density, momentum, turbulence viscosity discretization, turbulence kinetic energy, and turbulence dissipation rate discretization. The discretization system was solved using the coupled solver. Final convergence was obtained until the following criteria

were satisfied. The relative residuals for all flow variables were ≤ 10E-6, the mass flows across each face of the computation domain were stable, and the mass flow rate error was under 10E-6.

8. Validations of Numerical Simulation

The numerical simulation results were compared to the experimental results to validate the current study. **Table 3** compares the entrainment ratio and critical back pressure obtained from the numerical and experimental results at the nozzle throat diameter of 2.6 mm.

Table 3 Comparison between the numerical and the experimental results.

T_p (^oC)	T_s (^oC)	Critical back pressure (kPa)			Entrainment ratio		
		Exp	Num	Error %	Exp	Num	Error %
110	7.5	3.8	3.90	-2.63	0.26	0.263	-1.15
110	10	3.9	3.78	3.07	0.40	0.410	-2.5
120	10	5.4	5.52	-2.22	0.29	0.298	-2.75
130	10	7.2	7.38	-2.5	0.21	0.212	-0.95
120	15	5.8	5.62	3.10	0.40	0.420	-3.19
130	15	6.5	6.63	-2	0.30	0.311	-3.66

Figs. 8 and 9 show the numerical and experimental results for the Entrainment ratio and critical back pressure. It can be seen from these figures that the numerical results are very close to the experimental results. The maximum entrainment ratio deviation simulated was about -5.6%, while the critical back pressure deviation simulated was about 5.4%.

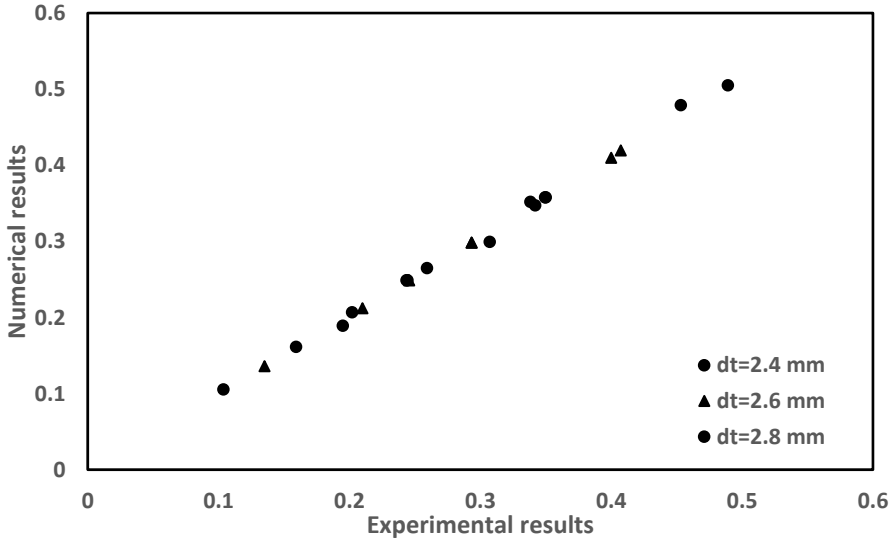

Figure 8. The numerical and experimental results for the entrainment ratio

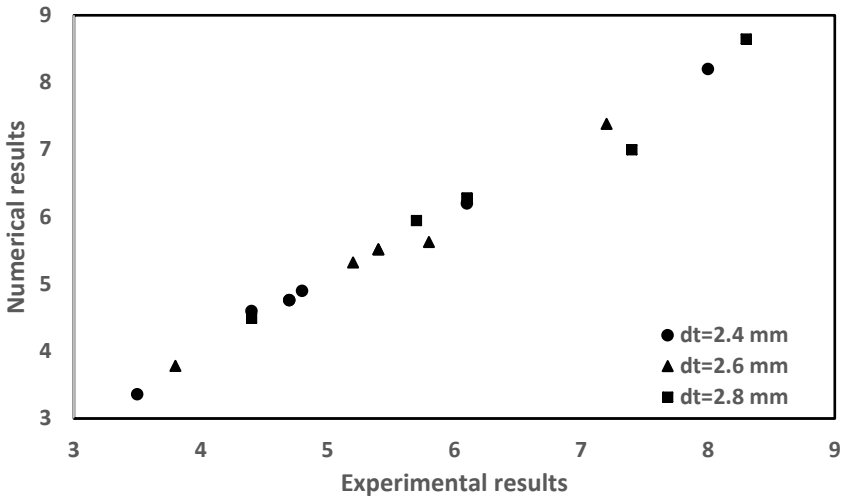

Figure 9. The numerical and experimental results for critical back pressure

9. RESULTS AND DISCUSSIONS

9.1 Experimental Results

Fig. 9 shows the impact of primary fluid temperature on the entrainment ratio. When the main fluid mass flow increases due to increased primary fluid temperature, the ejector entrains less evaporator fluid in the choked flow section. Because the flow area in the mixing chamber remains constant as the main fluid mass flow increases, the secondary fluid flow area (the annulus produced between the mixing chamber's wall and the center of the main fluid jet) decreases. The entrainment ratio will reduce when boiler pressure is raised. Increasing the primary fluid temperature from 110°C to 140°C (i.e., 27.27%) decreases the entrainment ratio by 66.25%.

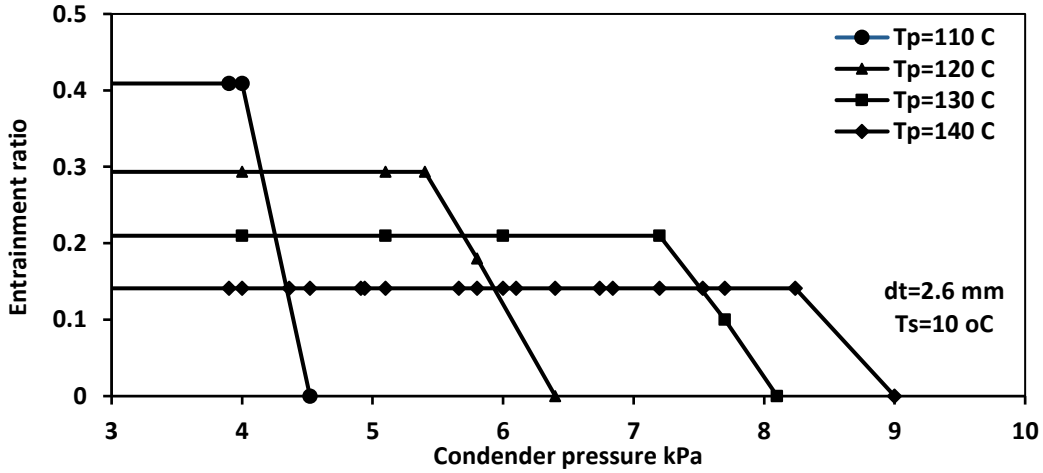

Figure 10. The variation of the entrainment ratio with the primary fluid temperature

Fig. 11 demonstrates the influence of secondary fluid temperature on the entrainment ratio. Increasing the evaporating temperature improves the entrainment ratio. This influence could be explained as when the primary fluid temperature is constant, increasing the

evaporating temperature raises the differential pressure between the secondary and the primary nozzle outlet. Therefore the sucked fluid flowing through the mixing chamber increases and causes the entrainment ratio to increase. Increasing the secondary fluid temperature from 7.5°C to 15°C (i.e., 100%) increases the entrainment ratio by 65.57%.

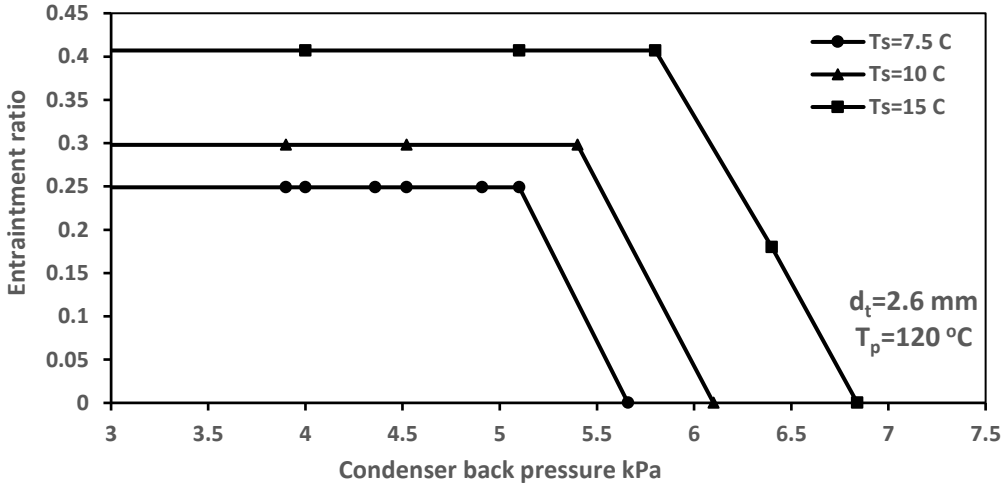

Figure 11. The variation of the entrainment ratio with the secondary fluid temperature

Fig. 12 shows the influence of the nozzle throat diameter on the entrainment ratio. It is clear that at fixed operation conditions, the entrainment ratio decreases almost with increased nozzle throat diameter since primary fluid mass flow increases. Increasing the nozzle throat diameter from 2.4 mm to 2.8 mm (i.e., 16.67%) decreases the entrainment ratio by 40 %.

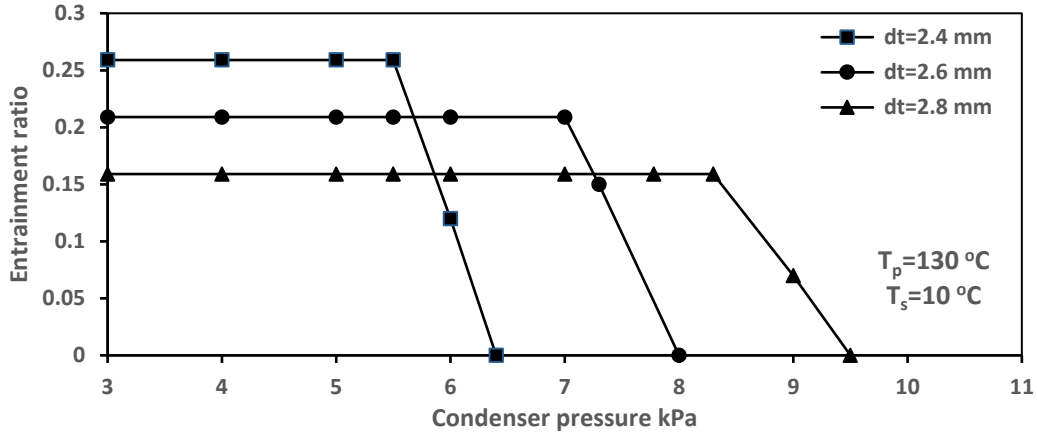

Figure 12. The variation of the entrainment ratio with the nozzle throat diameter

9.2 Numerical Results

9.2.1 Flow Form and Mixing Process in Ejector

Figs. 13 and 14 illustrate the contour lines of the Mach number and static pressure in the ejector generated by the CFD simulation. The main nozzle outlet Mach number is more significant than 4 for the configuration of the main nozzle used. When a fluid with high

temperature and pressure reaches the main nozzle, the primary nozzle's converging area causes the fluid to speed up. As the flow is choked at the throat of the main nozzle, the Mach number is one. Over-expanded waves are common when operating the ejector at a Mach number greater than 4. The first series of oblique shock waves represents the oblique shock observed in the extended wave. The flow form of the upstream fluids is regarded as a semi-separation, in which the pressure at the free boundary of the primary stream and the secondary stream is constant. These streams do not combine immediately after being mixed. As a result, the primary stream and the wall of the mixing chamber come together to produce the converging duct responsible for sucking the secondary fluid **(Kalkan et al., 2012)**

The shear stress layer forms at the interface between the main and secondary streams because of the significant velocity difference. Thus, the secondary fluid reaches supersonic speeds and chokes at a specific location along the converging duct. Choking of the secondary fluid occurs in an annular zone between the main jet's center and the wall of the mixing chamber, known as the effective area (A_e). When two fluids meet, a small quantity of the secondary fluid is gradually merged into the primary fluid upstream of the effective zone (Ae). When the secondary flow approaches sonic or chokes, all remaining components will be mixed. The operating pressure and ejector design make it difficult to determine where the effective zone is in the mixing chamber. Momentum is transferred from one fluid to another when two or more fluids are combined. The end effect is a reduction in the speed of the primary current, shown visually by a diamond wave's steady collapse.

Meanwhile, the secondary current is being progressively increased. Intense downstream pressure creates oblique shocks in the constant area section. The second shock refers to a second series of oblique shocks. These oblique shocks quickly raise the fluid's static pressure and supersonic flow changes to subsonic flow. Furthermore, the diffuser slows the flow before it enters the condenser.

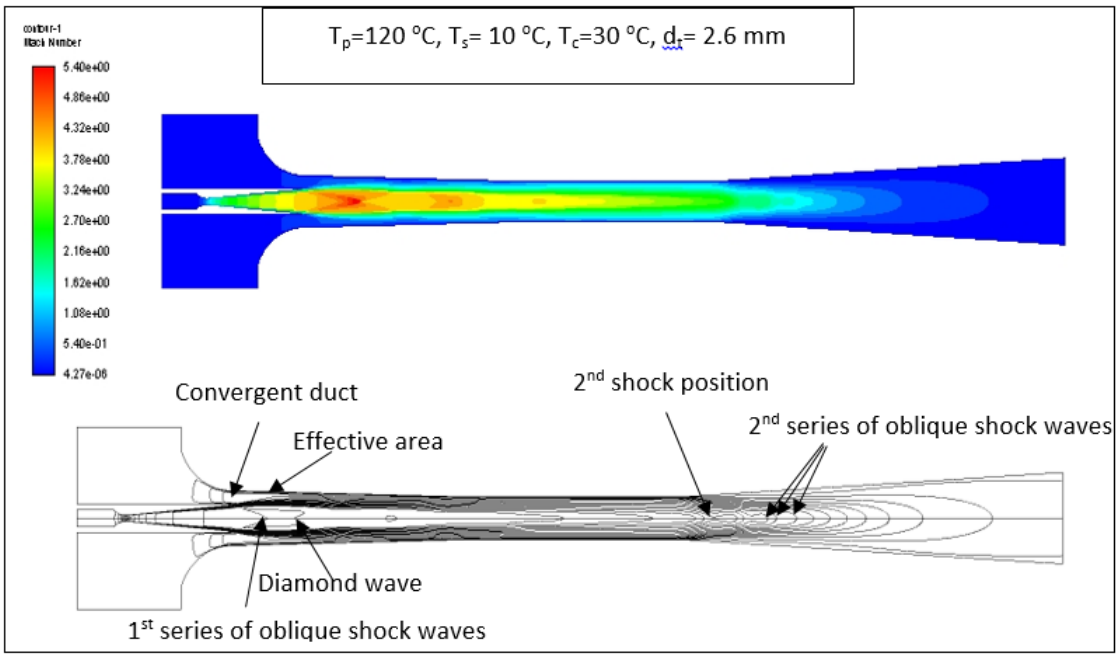

Figure 13. Mach number contours in the steam ejector

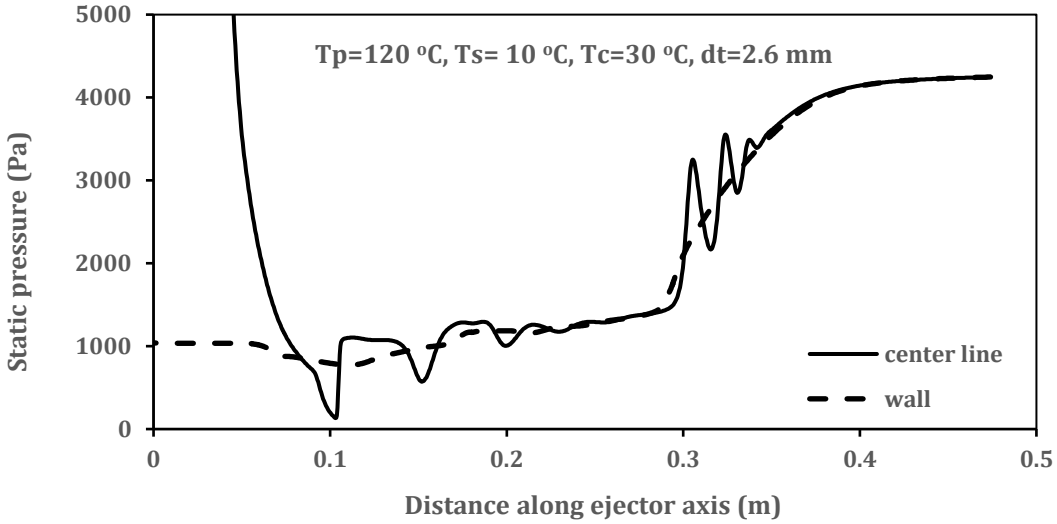

Figure 14. Static pressure along the centerline and wall of the steam ejector

9.2.2 Effect of Operation Conditions

Fig. 15 shows the influence of operation conditions (fluid temperature of primary and secondary streams and condenser pressure) on the entrainment ratio at a nozzle throat diameter of 2.4 mm for the numerical simulations and experimental results. As shown in **Fig.15**, the numerical simulation results are very close to the experimental results.

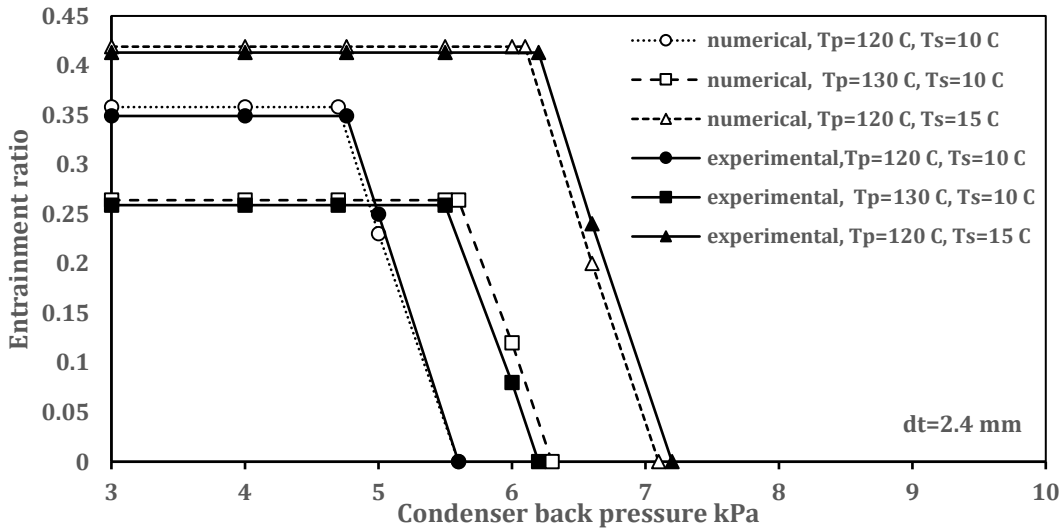

Figure 15. Influence of operation conditions on the Entrainment ratio for numerical and experimental results

The predicted CFD simulation entrainment ratio when the ejector's upstream and downstream pressures are adjusted is shown in **Fig. 16**. Depending on the primary and secondary fluid conditions, an ejector operates in three zones: choked, un-choked, and reversed flow. The same quantity of secondary vapor is sucked when the ejector runs at

critical back pressure. The entrainment rate decreases when the ejector runs after the critical condition as the back pressure increases. As the downstream pressure increased from A to D, the location of the second shock wave moved upstream into the ejector's throat.

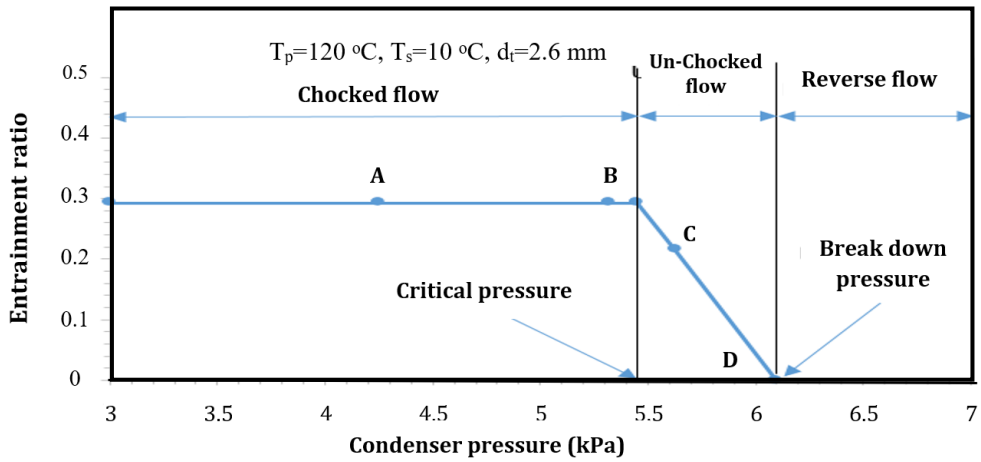

Figure 16. Performance characteristics of steam ejector based on the experimental results

9.2.2.1 Effect of the Condenser Pressure

Fig. 17 shows the complete Mach number contours through the ejector.

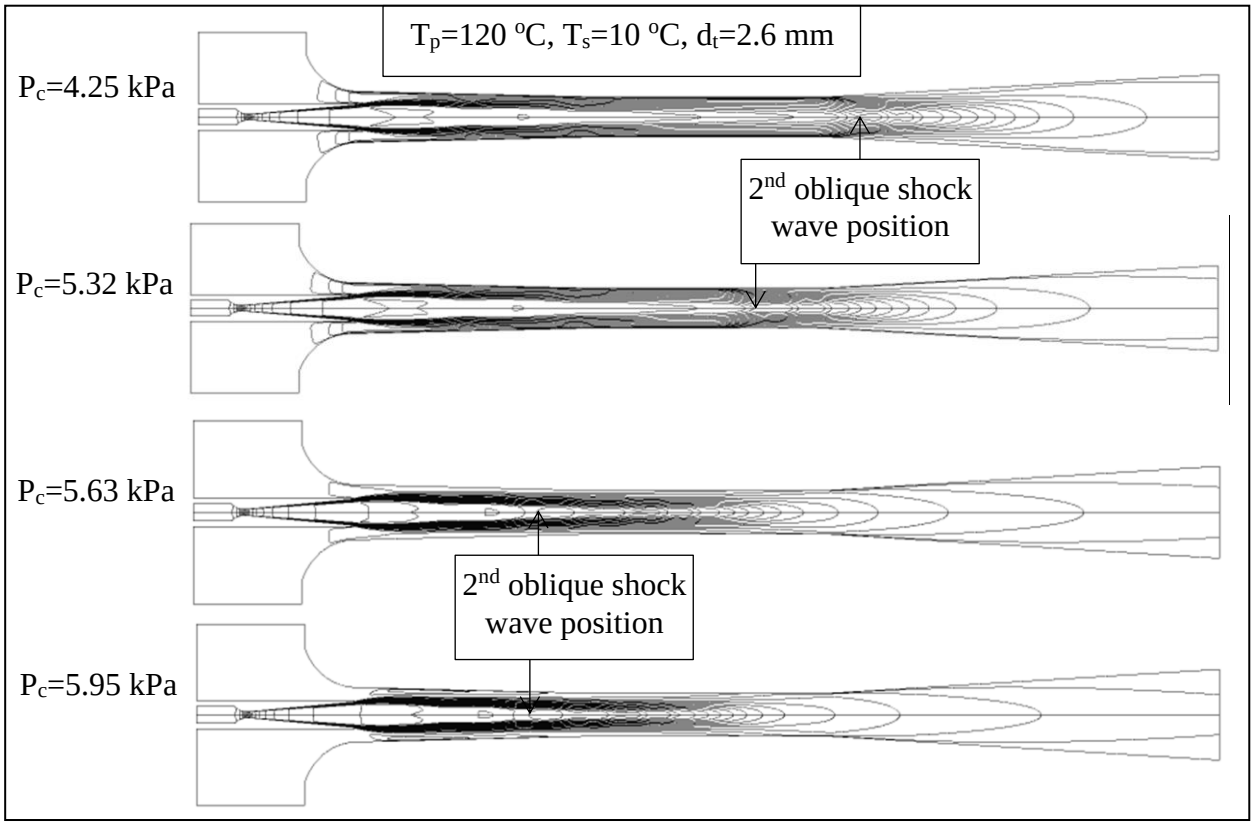

Figure 17. Effect of condenser back pressure on the Mach number contours.

Fig. 18 shows the static pressure profiles along the ejector's centerline. However, the shock does not influence the two streams (points A and B in **Fig. 16**) mixing behavior when the back pressure is less than the critical point. Since the entrainment ratio did not change, the primary stream kept the same size, and the effective area was always pushed to be in the constant area section. This causes the establishment of the choking phenomenon.
The oblique shocks' second series shifts upstream and merges with the oblique shocks' first series when the back pressure on the condenser is increased above the critical point (points C and D). The static pressure in the choking position rises above the critical value, and the secondary fluid is no longer choking. Once the oblique shocks' first series was no longer choking the secondary fluid, the sucking process was disturbed. This may be estimated by decreasing the secondary fluid and raising the static pressure before the shock. The primary fluid Mach number exiting a main nozzle is unaffected by increasing the primary fluid pressure. This follows the supersonic compressible flow concept; therefore, the flow rate and the fluid momentum are enhanced.

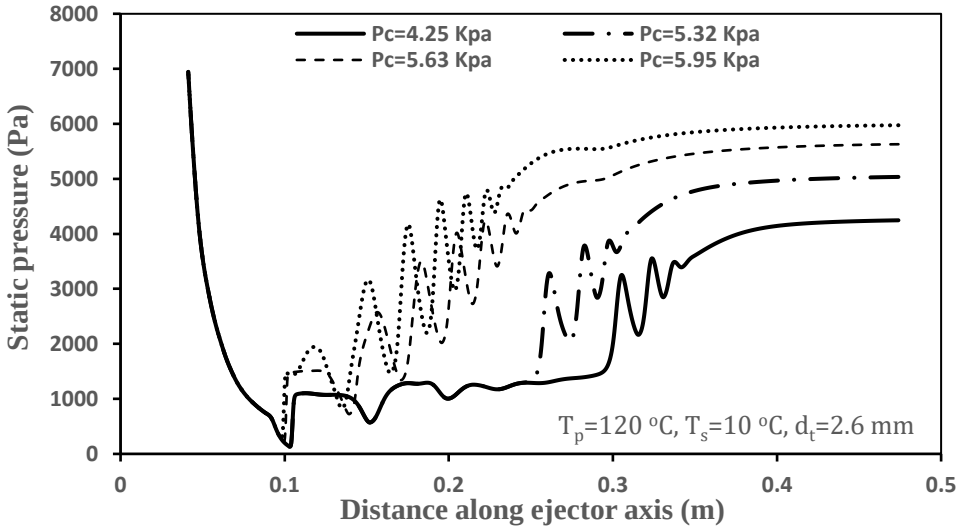

Figure 18. Effect of condenser back pressure on the static pressure distribution along the centerline of the steam ejector.

9.2.2.2 Effect of the Primary Steam Temperature

The primary fluid could exit, under-expand, and accelerate at a greater angle because of the additional momentum. **Figs. 19 and 20** show how the first oblique shock causes the flow to be shocked at a high Mach number. Increasing the jet's expansion angle makes the jet's core more prominent, reducing the annulus's effective area, the entrainment of secondary fluid, and the duct's higher gradient. The ejector can be run at a higher discharge pressure if the jet core velocity is raised since this causes the shock location to move downstream.

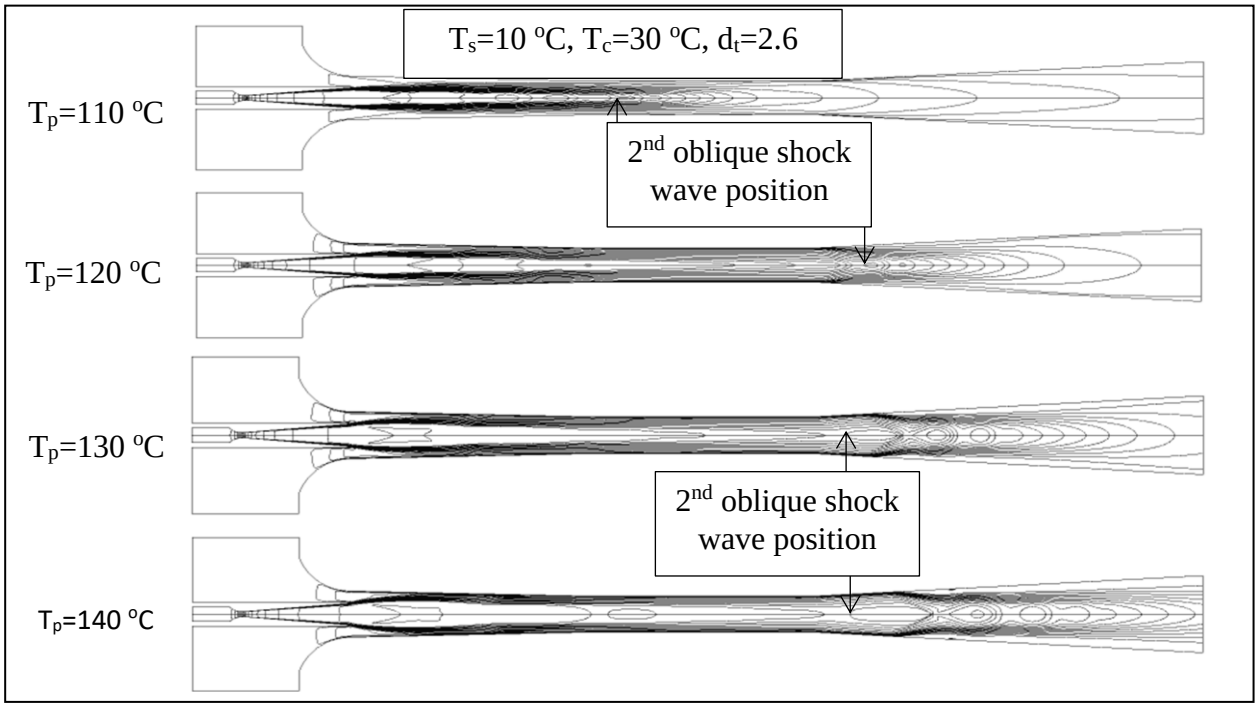

Figure 19. Effect of primary fluid temperature on the Mach number contours

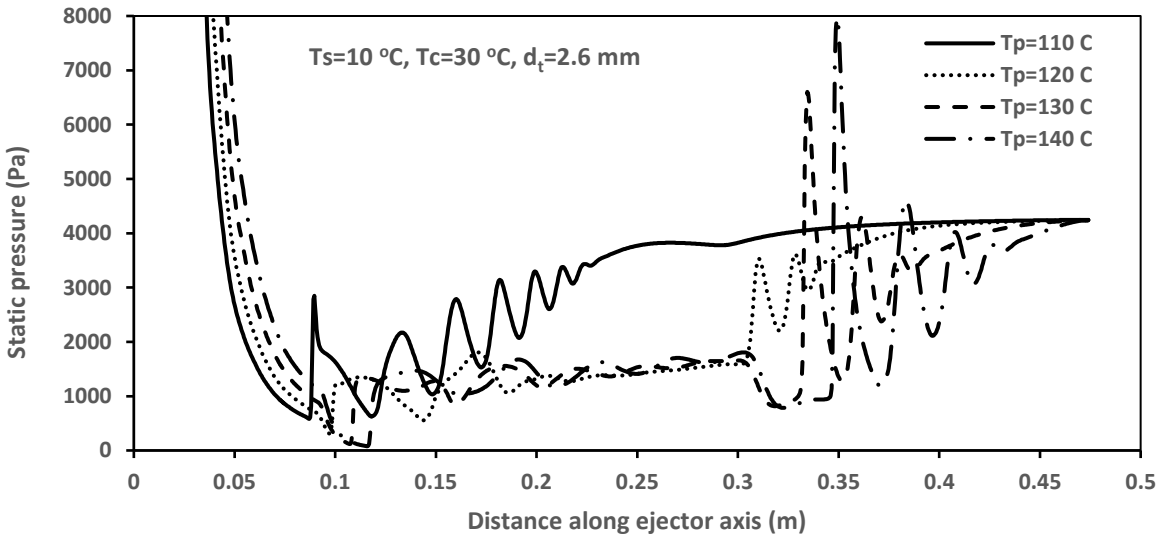

Figure 20. Effect of primary fluid temperature on the static pressure distribution along the steam ejector centerline

9.2.2.3 Effect of the Secondary Fluid Temperature

The contours of the Mach number in **Fig. 21** demonstrate how the secondary fluid temperatures affect the under-expanded wave's angle.

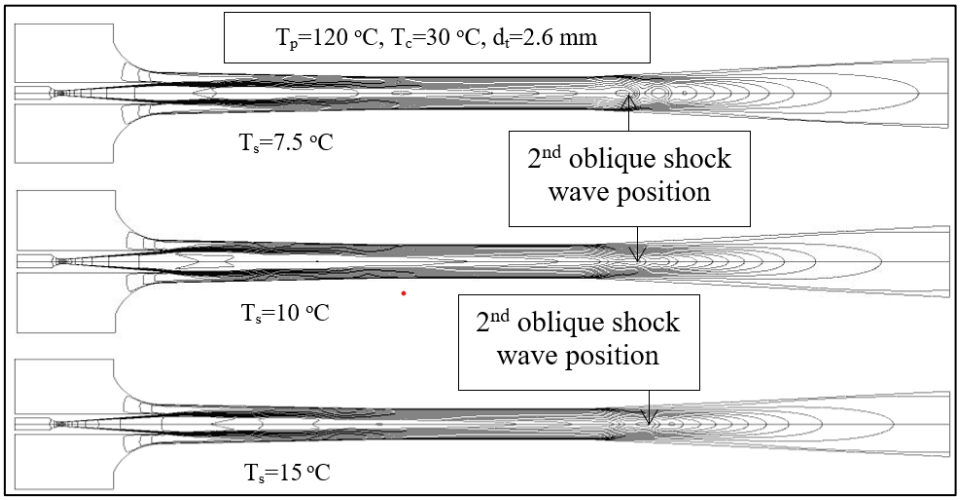

Figure 21. Effect of secondary fluid temperature on Mach number contours

The pressurized state led to a reduced jet core and increased effective area, which reduced the expansion angle. Lower Mach numbers resulted in more acceleration for the extended wave. Therefore, the jet core's momentum was decreased. However, if the converging duct's effective area is increased, more secondary fluid may be sucked and delivered. The jet core reduces the momentum of the mixed stream, balanced by the increased temperature of the secondary fluid. As the overall mixed stream momentum increases and the location of the shock wave shifts downstream, as shown in **Fig. 22**, it follows that the saturation temperature of the secondary fluid must also increase. Therefore, the ejector may operate at a higher downstream pressure.

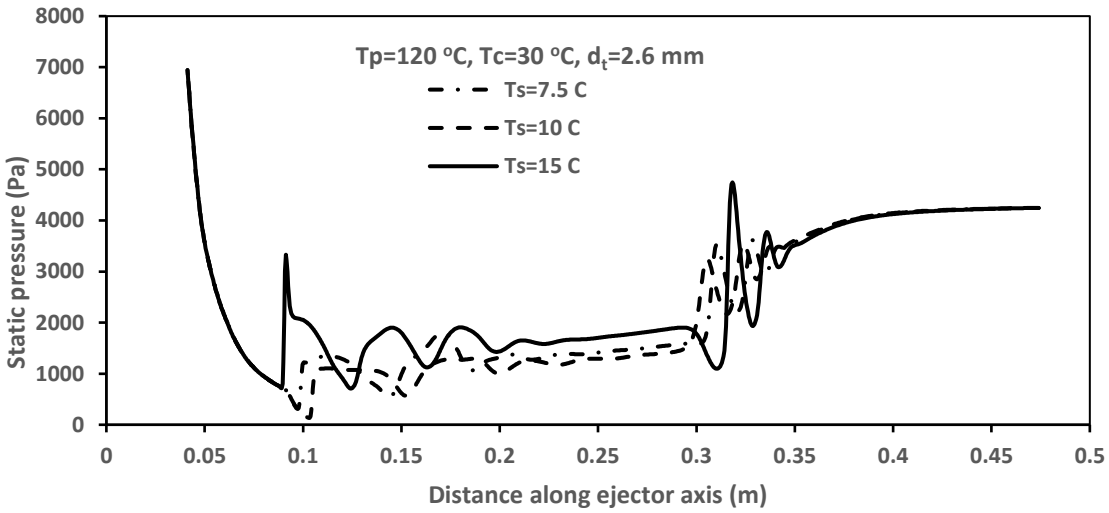

Figure 22. Effect of secondary fluid temperature on the static pressure distribution along the steam ejector centerline

9.2.3 Effect of Ejector Main Nozzle Throat Diameter

The performance of the steam ejector can be assessed by varying the main nozzle throat diameter under different operating situations. **Figs. 23 and 24** show the influence of the main nozzle throat diameter on Mach number contours and static pressure in the ejector.

The primary fluid mass flow rate is proportional to throat diameter for fixed boundary conditions. Consequently, the mainstream will have more momentum by increasing throat diameter. **Fig. 23** indicates that a more significant expanded-wave angle is created when the main nozzle has a larger throat diameter. The observation shows that the diameter of the throat is large. This results in a smaller secondary fluid effective area and a narrower converging duct. Although the same Mach number is produced at the jet's nozzle exit because of the same nozzle area ratio, the main flow expands more after exiting the nozzle. The enhanced momentum flow is responsible for these results. Increases in the throat diameter of the main nozzle lead to a reduction in the entrainment ratio because less secondary flow is sucked into the mixing chamber. As shown in **Fig. 24,** moving the second shock closer to the diffuser output allows the ejector to run at a higher critical back pressure.

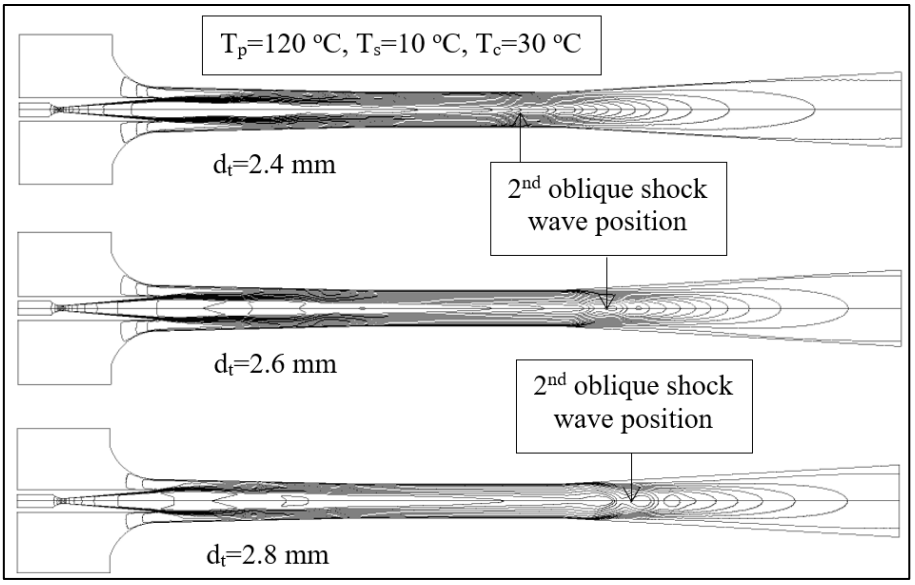

Figure 23. Influence of the main nozzle throat diameter on the Mach number contours

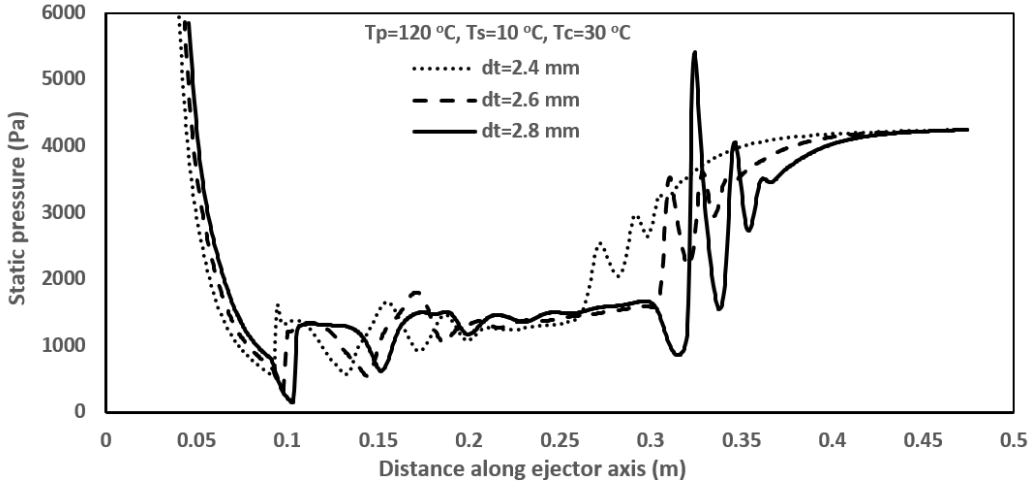

Figure 24. Effect of main nozzle throat diameter on static pressure distribution along the steam ejector centerline

10. CONCLUSIONS

The results of the numerical simulation and the experimental were investigated and compared. It was found that the entrainment ratio and critical back pressure obtained from the numerical approach were very close to the experimental results. The maximum entrainment ratio deviation simulated is about -3.66%, while the critical back pressure deviation is about 3.1%. The following is concluded from this study;

1- Increasing the primary fluid temperature, secondary fluid temperature, and nozzle throat diameter leads to moving the second shock wave toward the downstream (diffuser exit) direction.
2- Increasing condenser back pressure leads to moving the shock waves toward the upstream (main nozzle) direction.

It also can be concluded that the second shock series position detects the ejector operation mode. The ejector runs in critical mode if the second shock series position is close to the diffuser. In contrast, if the second shock series position moves towards the upstream, the ejector runs in subcritical mode. Finally, the ejector loses its capability to function correctly when the second shock wave series merges with the first. From this study, it can be concluded that the CFD technique can explain the mixing process and flow behavior inside the ejector, which cannot be demonstrated experimentally.

Nomenclature

Symbol	Description	Symbol	Description
Latin		**Greek**	
A	Area (mm^2)	μ	Dynamic viscosity Pa.s
D	Dimensional	ρ	Density, kg/m^3
d	Diameter, (mm)	τ	Turbulent shear stress
F	Force (N)	ω	Entrainment ratio
h	Height (m)	**Subscript**	
k	Thermal conductivity (W/m.K)	e	Evaporator, effective
ṁ	Mass flow rate (kg/sec)	ext	External
Ma	Mach number	p	Primary flow
R	Function	s	Secondary flow
P	Pressure, (kpa)	t	Nozzle throat
S_{ij}	Strain rate tensor	I,j	Index
t	Time (s)	Co	Ejector breakdown point
T	Temperature (^{o}c)	**Abbreviations**	
v	Independent parameter	CFD	Computational fluid difference
v	Velocity (m/s)	COP	Coefficient of performance
w	Uncertainty interval	Exp	Experimental
x	Coordinate	Num	Numerical

REFERENCES

Chen, J., 2014. Investigation of vapor ejectors in heat driven ejector refrigeration systems, Doctoral Thesis, Department of Energy Technology, Royal Institute of Technology, Stockholm, Sweden.

Chunnanond K., and Aphornratana S., 2004. Ejectors: applications in refrigeration technology. Renewable and Sustainable Energy Reviews, 8, pp. 129–155. Doi:10.1016/j.rser.2003.10.001

David Scott, Z., Ellache, O.B., and Ouzzane, M., 2008. CFD simulations of a supersonic ejector for use in refrigeration applications. *International Refrigeration and Air Conditioning Conference at Purdue*, pp. 14-17.

Diogo N.C., 2019. Development of a variable geometry ejector for a solar desalination systems. MSc. thesis, Mechanical Engineering department, University of Porto.

EZZAT Wali, 1980. *Optimum working fluids for solar powered Rankine cycle cooling of buildings*, Solar Energy, 25, pp. 235-24. Doi:10.1016/0038-092X(80)90330-8.

Ezzat, A.W., and Addaiy, R.M., 2010, Flash evaporation enhancement by electrolysis of saturated water flowing upwards in vertical pipe. *Journal of Engineering*, 16(3), pp. 5620-5632.

Federico, M., Dmitrii, B., Ilia, M., Nikolay, Z., and Adriano, M., 2016. Condensation in supersonic steam ejectors: comparison of theoretical and numerical models. 9th International Conference on Multiphase Flow, Italy.

Fletcher, C.A., 2013. *Computational techniques for fluid dynamics 1: Fundamental and general techniques*. Springer, Berlin, Heidelberg.

Galindo J., Dolz V., García L. M., and Alberto P., 2020. Numerical evaluation of a solar-assisted jet-ejector refrigeration system: Screening of environmentally friendly refrigerants. *Energy Conversion and Management*, 210, 112681. Doi:10.1016/j.enconman.2020.112681

Hart, J.H., 2002. Supersonic ejector simulation and optimisation. Ph.D. thesis, Department of Mechanical Engineering, University of Sheffield September.

Holman J. P., 2020. *Heat transfer*. 10th Edition, McGraw-Hill Higher Education.

Huang, B.J., Chang, J.M., Wang, C.P., and Petrenko, V.A., 1999. A1-D analysis of ejector performance. *International Journal of Refrigeration*, 22(5), pp. 354–364, Doi:10.1016/S0140-7007(99)0004-3.

Jamal, S., and Ezzat, A.W., 2021. *Investigation of evaporation and condensation process of induced flow using steam ejector. Journal of mechanics of continua and mathematical sciences*, 16(2). Doi:10.26782/jmcms.2021.02.00007

Jassim, N.A., and Abid, M.A., 2016. Modeling and simulation of thermal performance of solar-assisted air conditioning system under Iraq climate. *Journal of Engineering*, 22(8), pp. 175-194. Doi:10.31026/j.eng.2016.08.11

Kalkan N., Young E.A., and Celiktas A. 2012. Solar thermal air conditioning technology reducing the footprint of solar thermal air conditioning. Renewable and Sustainable Energy Reviews, 16, pp. 6352–83. Doi:10.1016/j.rser.2012.07.014

Kim D.S. and Infante F. C., 2008. Solar refrigeration options, a state-of-the-art review. *International Journal Refrigeration*, 31, pp. 3–15. Doi:10.1016/j.ijrefrig.2007.07.011 .

Luis P.L., Jose O., and Christine P., 2008. *A review on buildings energy consumption information. Energy and Buildings*, 40, pp. 394–398. Doi:10.1016/j.enbuild.2007.03.007.

Masoud, D., Seyedali, S., and Gerry, E. S., 2018. Geometrical optimization of a steam jet-ejector using the computational fluid dynamics. *Proceedings of the ASME*, 5, pp. 1-11. Doi:10.1115/FEDSM2018-83203

Matsuo K., Sasaguchi K., Kiyotoki Y., and Mochizuki H., 1982. Investigation of supersonic air ejectors (part 2, effects of throat-area ratio on ejector performance*). Bulletin of JSME*, 25(10), pp. 1898-1905. Doi:10.1299/jsme1958.25.1898

Megdouli K., Elakhdar, M., Nahdi, E., Kairouani, L., and Mhimid, A., 2015. Performance evaluation of a solar ejector-vapour compression cycle for cooling application*. Journal of Physics*, Conference Series 596, P. 012004. Doi:10.1088/1742-6596/596/1/012004.

Natthawut R.,Tongchana, T., Satha A., and Thanarath, S., 2013. CFD simulation on the effect of primary nozzle geometries for a steam ejector in refrigeration cycle. *International Journal of Thermal Sciences*, 63, pp. 133-145. Doi:10.1016/j.ijthermalsci.2012.07.009

Nguyen, V., and Vuaand, J.K., 2018. CFD simulation of ejector: is it worth to use real gas models?. *EPJ Web of Conferences,* 180, P. 02075. Doi:10.1051/epjconf/201818002075

Rashid, K.F., Hamakhan, I.A., and Mohammed, C.H., 2022. Dynamic simulation and optimization of flat plate solar collector parameters using the MATLAB program for Erbil-Iraq climate condition. *Al-Rafidain Engineering Journal*, 27(2), pp. 127-139. Doi: 10.33899/rengj.2022.133419.1167

Riffat, S.B., and Everitt, P., 1999. Experimental and CFD modelling of an ejector system for vehicle air conditioning. *Journal of the Institute of Energy*, 72, pp. 41-47.

Robert Nichols, 2010. *Turbulence models and their application to complex flows*. University of Alabama at Birmingham. https://overflow.larc.nasa.gov/wp-content/uploads/sites/54/2014/06/Turbulence_Guide_v4.01.pdf

Sokolov, M., and Hershgal, D., 1990. Enhanced ejector refrigeration cycles powered by low grade heat. Part 1 Systems characterization*. International Journal Refrigeration*, 13, P. 351. Doi:10.1016/0140-7007(90)90023-P

Sriveerakul, T., Aphornratana, S., and Chunnanond, K., 2007. Performance prediction of steam ejector using computational fluid dynamics: Part 2. Flow structure of a steam ejector influenced by operating pressures and geometries. *International Journal of Thermal Sciences*, 46, pp. 823–833. Doi:10.1016/j.ijthermalsci.2006.10.012

Sun D.W., 1999. Comparative study of the performance of an ejector refrigeration cycle operating with various refrigerants. *Energy Conversion & Management*, 40, pp. 873–884. Doi:10.1016/S0196-8904(98)00151-4.

Suvarnakuta, N., Pianthong, K., Sriveerakul, T., and Seehanam, W., 2020. Performance analysis of a two-stage ejector in an ejector refrigeration system using computational fluid dynamics. *Engineering*

Applications Of Computational Fluid Mechanics, 14(1), pp. 669–682. Doi:10.1080/19942060.2020.1756913

Varga, S., Oliveira, A., Ma, X., Omer, S., Zhang, W., and Riffat, S., 2012. Comparative study of the performance of a variable area ratio steam ejector. 15th International Conference on Experimental Mechanics, 3179, Faculty of Engineering, University of Porto, Portugal, 22-27 July.

Wenxu, S., Xiaojing, M., Yuanmin, Z., Lei, J., and Haoyuan, X., 2021. Performance analysis and optimization of a steam ejector through streamlining of the primary nozzle. *Case studies in thermal engineering*, 27, P. 101356. Doi:10.1016/j.csite.2021.101356

Yapıcıa, R., Ersoya, H.K., Aktoprakoglua, A., Halkacıa, H.S., and Yigitb, O., 2008. Experimental determination of the optimum performance of ejector refrigeration system depending on ejector area ratio. *International journal of refrigeration*, 31, pp. 1183 – 1189. Doi:10.1016/j.ijrefrig.2008.02.010.

Yu, H., Lixin, G., Xiaodong, W., Anthony, C.Y., Cuiling, L., Ruifeng, C., Hengrui, L., Tim, B.Y., Jiyuan, T., and Guan, H.Y., 2019a. A steam ejector refrigeration system powered by engine combustion waste heat: part 2. Understanding the nature of the shock wave structure. *Appl. Sci*., 9, pp. 4435. Doi:10.3390/app9204275

Yu, H., Xiaodong W., Hao S., Guangli Z., Lixin G., and Jiyuan T., 2019b. CFD simulation on the boundary layer separation in the steam ejector and its influence on the pumping performance, *Energy*, 167, pp. 469-483. Doi:10.1016/j.energy.2018.10.195.